Homochiral lanthanoid(III) mesoxalate metal–organic frameworks: synthesis, crystal growth, chirality, magnetic and luminescent properties†

Beatriz Gil-Hernández,[a] Jana K. Maclaren,[b] Henning A. Höppe,[c] Jorge Pasán,[d] Joaquín Sanchiz*[a] and Christoph Janiak*[e]

The achiral chelating and bridging mesoxalato ligand (H_2mesox^{2-}), the conjugate base of mesoxalic or dihydroxymalonic acid (H_4mesox), is a new enantiopurity enforcer in extended structures by yielding the Λ/Δ-metal configured homochiral MOFs 2D-[$Ln_2(\mu\text{-}H_2mesox)_3(H_2O)_6$], [with Ln(III) = La (**1**), Ce (**2**), Pr (**3**), Nd (**4**), Sm (**5**), Eu (**6**), Gd (**7**), Tb (**8**), Dy (**9**), Er (**10**) and Yb (**11**)]; through self-resolution during crystallization. Single crystals of the compounds have been grown in agarose gel. All the compounds obtained are isostructural as deduced by means of single crystal and powder X-ray diffraction analysis and exhibit the Ln(III) ions covalently connected by the mesoxalato ligands into a corrugated grey arsenic-type (6,3)-net (or layer) with chair-shaped six-membered rings. Luminescence measurements reveal that the Eu(III) compound (**6**) exhibits several strong characteristic emission bands for isolated europium(III) ions in the visible region when excited between 350 and 420 nm; similarly the terbium(III) compound (**8**) displays the characteristic emission bands for isolated terbium(III) ions. Magnetic susceptibility measurements show deviations from the Curie law mainly owing to the split of the ground term due to the ligand field and spin–orbit coupling in the case of Sm(III) (**4**) and Eu(III) (**6**) compounds.

Introduction

The combination of lanthanoid(III) ions with carboxylate-containing bridging ligands has produced a great variety of extended metal–organic frameworks (MOFs) which are of special importance since they exhibit interesting properties such as porosity, luminescence, magnetism, catalytic activity and chirality.[1–15] The synthesis of chiral materials is of particular attention since they may lead to enantioselective catalysis,[16] or to the exhibition of singular properties, such as magneto-chirality.[17–19] The synthesis of chiral MOFs can be induced by chiral templating or by the use of chiral ligands. Also, homochiral MOFs are prepared from totally achiral components *via* spontaneous resolution during crystal growth.[16] In this approach a stereogenic center must be created in the complexation of the metal ions by the achiral ligands in the construction and crystallization of the MOF. If all the metal centers in the crystal keep the same Λ- or Δ-configuration the crystal will be chiral, the reaction yielding equivalent quantities of both crystal enantiomorphs (opposite handedness) of MOFs. We have followed this strategy for the synthesis of 2D-[$Ln_2(\mu\text{-}H_2mesox)_3(H_2O)_6$] (**1–11**) in which the doubly deprotonated dinegative mesoxalato ligands assemble only metal centers of the same Λ- or Δ-configuration within a single crystal. We present here in, as a continuation of our work with the

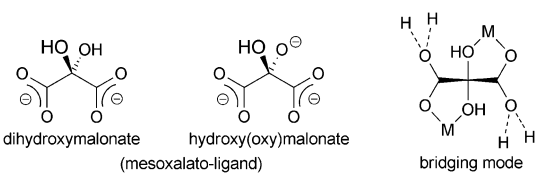

Scheme 1 Left: di-negative doubly deprotonated mesoxalato ligand. Middle: tri-negative triply deprotonated mesoxalato ligand. Right: bis-chelating bridging mode of the di-negative mesoxalato ligand, dotted line represents the hydrogen bonds from the C–OH groups of the neighboring mesoxalato ligand and the H-atoms of aqua ligands.

[a]*Grupo de Materiales Magnéticos, Departamento de Química Inorgánica, Universidad de La Laguna, 38206 La Laguna, Tenerife, Spain. E-mail: beagher@ull.es; jsanchiz@ull.es*

[b]*Institut für Anorganische und Analytische Chemie, Universität Freiburg, Albertstr. 21, 79104 Freiburg, Germany. E-mail: janak.maclaren@googlemail.com*

[c]*Institut für Physik, Universität Augsburg, Universitätsstraße 1, D-86159 Augsburg, Germany. E-mail: henning@ak-hoeppe.de*

[d]*Laboratorio de Rayos X y Materiales Moleculares, Departamento de Física Fundamental II, Facultad de Física, Universidad de La Laguna, Av. Astrofísico Francisco Sánchez s/n, 38206 La Laguna, Tenerife, Spain. E-mail: jpasang@ull.es*

[e]*Institut für Anorganische Chemie und Strukturchemie, Universität Düsseldorf, 40204 Düsseldorf, Germany. E-mail: janiak@uni-duesseldorf.de*

† Electronic supplementary information (ESI) available. CCDC reference numbers 780266 and 853393–853398. For ESI and crystallographic data in CIF or other electronic format see DOI: 10.1039/c2ce06496k

mesoxalate ligand (Scheme 1),[20–22] their synthesis, crystal growth, the structure, the magnetic and luminescent properties.

Experimental

Mesoxalic acid, lanthanoid(III) nitrates hexahydrate and agarose were purchased from commercial sources and used as received. Elemental analyses (C and H) were performed on an EA 1108 CHNS-O microanalytical analyzer. IR spectra (400–4000 cm^{-1}) were recorded on a Thermo Nicolet Avatar 360 FT-IR spectrometer with the sample prepared as KBr pellets.

Preparation of catena-Λ/Δ-[triaqua-1.5(μ-dihydroxymalonato-κO,O′:O″,O‴) lanthanoid(III)] (1–11)

Polycrystalline samples of the compounds 2D-[Ln_2(μ-H_2mesox)$_3$(H_2O)$_6$] [with Ln = La (**1**), Ce (**2**), Pr (**3**), Nd (**4**), Sm (**5**), Eu (**6**), Gd (**7**), Tb (**8**), Dy (**9**), Er (**10**), Yb (**11**)] were prepared by a standard procedure. An aqueous solution of 2-dihydroxymalonic acid (0.3 mmol in 3 mL) was placed in a sample tube and an aqueous solution of the lanthanoid(III) nitrate hexahydrate (0.2 mmol in 3 mL) was added with a Pasteur pipette from the bottom of the tube without mixing both solutions in order to perform a slow diffusion experiment. A small amount of precipitate was formed immediately, which was allowed to stand. Following this procedure X-ray suitable single crystals were obtained for La(III) compound (**1**). A polycrystalline material was obtained for the rest of lanthanoids, which was used for the X-ray powder diffraction, magnetic and luminescent (Eu and Tb) measurements. In order to obtain single crystals of compounds **2–11** crystallization in agarose gel was performed. Agarose (10 mg) was added to an aqueous solution of the lanthanoid(III) nitrate hexahydrate (0.2 mmol in 5 mL) placed in a test tube and then heated to 90 °C in a water bath under stirring. The solution was allowed to cool to room temperature and once the gel was formed, an aqueous solution of 2-dihydroxymalonic acid (0.3 mmol in 5 mL) was added above and allowed to crystallize at room temperature. X-Ray suitable single crystals of compounds **2–11** were obtained within a week. Elemental analyses (C and H) are shown in Table S1 of the ESI† and IR spectra in Fig. S1 of the ESI†.

X-Ray crystallography and physical measurements

X-Ray crystallography. Suitable single crystals were carefully selected under a polarizing microscope.

Data collection. The crystallographic data for the single crystals of **2** were collected at 293(2) K on a Nonius Kappa CCD diffractometer with graphite-monochromated Mo-Kα radiation (λ = 0.71073 Å). Orientation matrix and lattice parameters were determined by least-squares refinement of the reflections obtained by a θ–χ scan (Dirac/lsq method). Data collection and data reduction of **2** were performed with the COLLECT and EVALCCD programs. For compounds **1**, **3**, **4**, **7**, **10** and **11** the crystals were measured on either a Rigaku *R*-axis Spider image plate detector or a Bruker AXS with Apex II CCD area-detector diffractometer (specified in Table 1). Rigaku Spider: Mo-Kα radiation (λ = 0.71073 Å), graphite monochromator, double-pass method ω-scan; data collection, cell refinement and data reduction with CrystalClear,[23] empirical (multi-scan) absorption correction with ABSCOR.[24] Bruker AXS: Mo-Kα radiation (λ = 0.71073 Å), graphite monochromator, ω-scans, data collection with APEX2,[23,25] cell refinement and data reduction with SAINT, experimental absorption correction with SADABS.[26]

Structure analysis and refinement. The structures were solved by direct methods (SHELXS-97), refinement was done by full-matrix least squares on F^2 using the SHELXL-97 program suite.[31,32] All non-hydrogen positions were refined with anisotropic temperature factors. Hydrogen atoms of the aqua ligands and on the hydroxyl groups of the mesoxalato ligand were found and refined with $U_{iso}(H) = 1.5\ U_{eq}(O)$. Crystal data and details concerning the structure refinement are given in Table 1. Computations on the supramolecular interactions were carried out with PLATON for Windows.[33] Graphics were drawn with DIAMOND (Version 3.2).[34]

Powder X-ray diffraction data. Powder X-ray diffraction data were collected in the range $5° < 2\theta < 60°$ on a PANalytical X'pert X-ray diffractometer (Cu-Kα radiation $\lambda_\alpha = 1.54184$ Å) at room temperature for all the compounds. The powder diffraction patterns indicate that all of them are isostructural (Fig. S2, ESI†).

Magnetic susceptibility measurements. Magnetic susceptibility measurements were carried out on polycrystalline samples by means of a Quantum Design SQUID magnetometer. The *dc* measurements were performed in the temperature range 1.9–300 K at applied magnetic fields of 1000 Oe for $T < 15$ K and 10 000 Oe for $T > 10$ K. Diamagnetic corrections of the constituent atoms were estimated from Pascal's constants and experimental susceptibilities were also corrected for the magnetization of the sample holder.

Photoluminescence analyses. Photoluminescence analyses for the europium and terbium compounds were conducted on powdered samples at room temperature in diffuse reflection geometry on a Horiba Fluoromax4 fluorescence spectrometer equipped with a Xe discharge lamp. The acquisition time was 1 nm s^{-1}.

Results and discussion

Structure of the compounds

The compounds 2D-[Ln_2(μ-H_2mesox)$_3$(H_2O)$_6$] with Ln(III) = La (**1**), Ce (**2**), Pr (**3**), Nd (**4**), Sm (**5**), Eu (**6**), Gd (**7**), Tb (**8**), Dy (**9**), Er (**10**), Yb (**11**) are all isostructural and crystallize in the space group *R*32 (no. 155). For seven of these compounds (**1**, **2**, **3**, **4**, **7**, **10** and **11**) single crystals of sufficient quality could be obtained and measured.

Three doubly deprotonated, di-negative mesoxalato (dihydroxymalonate) ligands chelate the Ln(III) atoms through one carboxylate oxygen atom and the hydroxyl oxygen atom (Scheme 1). Three aqua ligands then complete the Ln coordination polyhedron to a tri-capped (slightly distorted) trigonal prism. From the caps, the mesoxalato ligand chelates down to the "base" of the prism. Strong "charge assisted" H-bonds[20,35–47]

Table 1 Crystal data and structure refinement for **1–11**

Metal, compound	La (**1**)	Ce (**2**)	Pr (**3**)	Nd (**4**)	Gd (**7**)	Er (**10**)	Yb (**11**)
Empirical formula	$C_9H_{18}La_2O_{24}$	$C_9H_{18}Ce_2O_{24}$	$C_9H_{18}O_{24}Pr_2$	$C_9H_{18}Nd_2O_{24}$	$C_9H_{18}Gd_2O_{24}$	$C_9H_{18}Er_2O_{24}$	$C_9H_{18}O_{24}Yb_2$
M/g mol^{-1}	788.05	790.47	792.05	798.71	824.73	844.75	856.31
Crystal size/mm^3	0.38 × 0.29 × 0.28	0.15 × 0.15 × 0.15	0.15 × 0.10 × 0.10	0.12 × 0.10 × 0.09	0.19 × 0.10 × 0.08	0.32 × 0.19 × 0.11	0.20 × 0.15 × 0.10
Temperature/K	123(2)	293(2)	294(2)	203(2)	294(2)	203(2)	203(2)
θ range/° (completeness)	4.18–39.99 (98.8%)	4.19–30.49 (99.1%)	4.18–35.00 (98.3%)	2.91–36.12 (98.6%)	4.23–33.14 (99.6%)	2.65–34.49 (97.1%)	2.66–36.25 (97.3%)
h; k; l range	±17; ±17; −35, 37	−12, 13; −13, 10; −30, 29	±15; ±15; ±34	−15, 14; −16, 15; −34, 32	±14; −13, 12; −31, 29	−15, 14; ±15; −30, 32	±15; ±15; −32, 33
Crystal system	Trigonal	Trigonal	Trigonal	Trigonal	Trigonal	Trigonal	Trigonal
Space group	*R*32	*R*32	*R*32	*R*32	*R*32	*R*32	*R*32
$a = b$/Å	9.75040(10)	9.7193(14)	9.7612(4)	9.69740(10)	9.6396(8)	9.5813(2)	9.55480(10)
c/Å	21.2854(15)	21.1909(42)	21.3097(9)	20.9760(5)	20.7433(16)	20.4715(6)	20.4006(4)
$\alpha = \beta$/°	90	90	90	90	90	90	90
γ/°	120	120	120	120	120	120	120
V/Å^3	1752.50(13)	1733.6(5)	1758.39(13)	1708.30(5)	1669.3(2)	1627.53(7)	1612.93(4)
Z	3	3	3	3	3	3	3
D_{calc}/g cm^{-3}	2.240	2.271	2.244	2.329	2.461	2.586	2.645
μ/mm^{-1}	3.714	3.997	4.213	4.618	6.020	7.796	8.759
F(000)	1134	1140	1146	1152	1176	1200	1212
Max./min. transmission	0.4228/0.3327	0.5855/0.5855	0.6780/0.5706	0.6813/0.6072	0.6445/0.3942	0.4809/0.1893	0.4746/0.2733
Reflections collected	46 805	6225	17 384	20 229	10 169	13 137	21 721
Indep. refl. (R_{int})	2409 (0.0145)	1179 (0.0160)	1688 (0.0261)	1783 (0.0307)	1425 (0.0346)	1480 (0.0255)	1696 (0.0252)
Data/restraints/ parameters	2409/5/63	1179/5/63	1688/5/63	1783/5/63	1425/5/63	1480/5/63	1696/4/63
Max./ min. $\Delta\rho^a$/eÅ^{-3}	1.263/−1.246	0.811/−0.737	0.558/−0.689	0.915/−0.723	0.834/−0.959	1.679/−2.219	1.263/−1.626
$R1$/w$R2$ $[I > 2\sigma(I)]^b$	0.0125/0.0296	0.0127/0.0358	0.0145/0.0274	0.0146/0.0292	0.0179/0.0391	0.0132/0.0357	0.0132/0.0366
$R1$/w$R2$ (all reflect.)^b	0.0126/0.0297	0.0133/0.0361	0.0156/0.0276	0.0160/0.0296	0.0187/0.0394	0.0133/0.0357	0.0137/0.0367
Goodness-of-fit on F^{2c}	1.189	1.202	1.176	1.054	1.190	1.230	1.276
Flack parameter^d	−0.004(11)	0.007(19)	−0.007(12)	−0.004(12)	−0.027(16)	0.012(12)	0.010(11)
Diffractometer	Rigaku Spider	Nonius Kappa	Rigaku Spider	Bruker AXS	Rigaku Spider	Bruker AXS	Bruker AXS

^{a} Largest difference peak and hole. ^{b} $R1 = [\Sigma(||F_o| - |F_c||)/\Sigma|F_o|]$; $wR2 = [\Sigma[w(F_o^2 - F_c^2)^2]/\Sigma[w(F_o^2)^2]]^{1/2}$. ^{c} Goodness-of-fit $= [\Sigma[w(F_o^2 - F_c^2)^2]/(n-p)]^{1/2}$. ^{d} Absolute structure parameter.[27–30]

between neighboring mesoxalato ligands from the coordinated (CO–)H atom to an uncoordinated carboxylate O-atom are probably important for the ligand orientation around the metal atom. The "top" of the prism is formed by the three aqua ligands (Fig. 1 and 2).

The Ln atom sits on a three-fold proper rotation axis and the ligand central carbon atom sits on a two-fold proper rotation axis. Therefore only one aqua ligand and half a mesoxalato ligand are crystallographically unique (Fig. 1). Depending on the crystal investigated the chelate-ring planes of the three mesoxalato ligands constitute either a left- or right handed propeller around each Ln atom, akin to the Λ- or Δ-metal-centered chirality in an octahedron (Fig. 2).

The non-centrosymmetric Sohncke[48] space group *R*32 lacks inversion symmetry. For a given single crystal only the Δ- or Λ-configuration can be found as based on the absolute structure or Flack parameter of less than 0.03 (*cf.* Table 1).[27–30] Such a Flack parameter close to zero confirms the correct absolute structure. In combination with other refinement parameters and with normal atom temperature factors such as the absence of

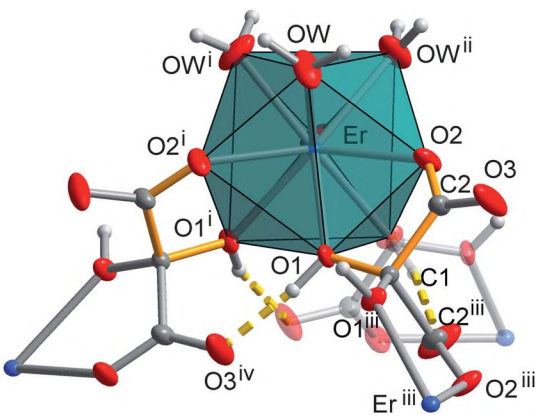

Fig. 1 The ligand configuration around Er(III) (chosen as the representative example) in a polyhedral illustration to show the tri-capped trigonal prism. To highlight the Δ-configuration the chelating part of the ligand is presented with orange bonds. The bridging function of the ligand is also indicated. Intra-layer H-bonds around the metal atom are shown as yellow dashed lines. Thermal ellipsoids are 80% for all atoms; H atoms with arbitrary radii. Symmetry transformations: i = $-y$, $x - y$, z; ii = $-x + y$, $-x$, z; iii = $1/3 + x - y$; $2/3 - y$, $2/3 - z$, iv = $-2/3 + y$, $-1/3 + x$, $2/3 - z$. Selected bond lengths and angles are given in Table 2.

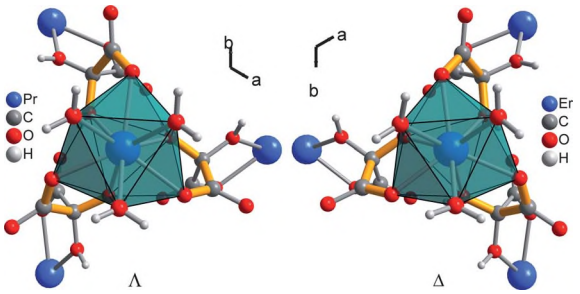

Fig. 2 The Λ-configuration around Pr(III) and the Δ-configuration around Er(III) (chosen as representative examples). To highlight the Λ- and Δ-configuration the chelating part of the ligand is presented with orange bonds. H-bonds are not shown for clarity.

molecular disorder, no significant amount of complexes with the opposite metal chirality (*i.e.*, an enantiomer mixture) is present within one of the investigated crystals. Thus, the crystallization of a single crystal proceeds enantioselective to give either Λ- or Δ-metal-centered chirality within one single crystal. This enantioselectivity renders each single crystal homochiral (enantiopure). However, the batch most likely contains both enantiomorphs and the overall crystal mixture should be racemic.[20,21,49,50] The special name racemic conglomerate is given to the crop of crystals grown under equilibrium conditions from a racemate undergoing spontaneous resolution.[48,51–54] Five different crystals of the La compound **1** were measured to find both enantiomers. This procedure was, however, not repeated for the other compounds. Overall 5 crystals with Λ-configuration and 6 with Δ-configuration were measured for **1–11**, namely for La (**1**) one Λ and four Δ, Ce (**2**) Λ, Pr (**3**) Λ, Nd (**4**) Λ, Gd (**7**) Λ, Er (**10**) Δ and Yb (**11**) Δ. Each mesoxalato ligand bridges between two Ln atoms in a bis-chelating fashion. These bis-chelate bridges involve both ends of the mesoxalato ligand, forming two five-membered chelate rings (Scheme 1, Fig. 1 and 2). This way, it can be reasoned that the mesoxalato ligands connect only Ln atoms of the same handedness (Λ- or Δ-configuration) to a corrugated grey arsenic-type (6,3)-net.[55,56] This neutral 2D-[Ln_2(mesox)$_3$] net consists of chair-shaped six-membered rings (Fig. 3 and 4). The layers are connected by strong "charge assisted" H-bonds[20,35–47]

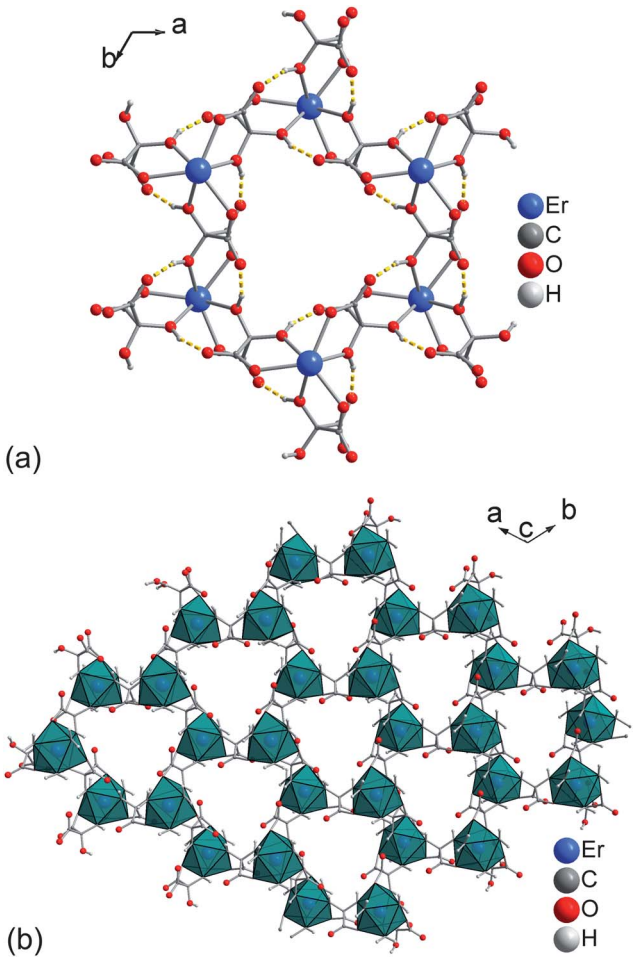

Fig. 3 Chair-shaped six-membered rings through the ligand bridging action with the hydrogen bonds around the metal atom as yellow dashed lines (aqua ligands omitted for clarity) (a) leading to a corrugated gray-arsenic type (6,3)-net (b). Compound **10** was chosen as an example.

from the aqua ligands to uncoordinated carboxylate O-atoms of the mesoxalato ligand in the adjacent net (*cf.* Fig. 6). Through these H-bonds, adjacent layers combine to a 3D

Table 2 Selected bond lengths (Å) and angles (°) in **1–11**[a]

Metal, compound	Λ-La, **1**	Λ-Ce, **2**	Λ-Pr, **3**	Λ-Nd, **4**	Λ-Gd, **7**	Δ-Er, **10**	Δ-Yb, **11**
M–O1	2.5739(8)	2.5532(15)	2.5566(11)	2.5213(11)	2.4730(19)	2.4305(16)	2.4152(15)
M–O2	2.5175(10)	2.4903(18)	2.4897(13)	2.4673(13)	2.422(2)	2.3831(18)	2.3687(17)
M–OW	2.4994(11)	2.477(2)	2.4813(14)	2.4412(14)	2.392(2)	2.3357(19)	2.3153(18)
O1–M–O2	60.15(3)	60.48(5)	60.92(4)	61.27(4)	62.32(6)	63.33(5)	63.60(5)
O1–M–OW	94.58(4)	93.96(8)	93.90(5)	93.17(5)	92.20(9)	91.33(7)	91.09(7)
O2–M–OW	76.17(4)	75.27(8)	74.95(6)	74.60(5)	73.23(9)	72.75(7)	72.51(7)
O1–M–O1^{i}	71.57(3)	71.89(6)	72.01(4)	72.50(4)	73.29(7)	73.95(6)	74.00(6)
O2–M–O2^{i}	119.285(7)	119.394(11)	119.503(7)	119.593(7)	119.791(8)	119.881(5)	119.896(5)
OW–M–OW^{i}	73.66(5)	74.14(10)	74.09(7)	74.72(6)	75.23(11)	75.80(9)	76.05(8)
H-bonds							
O1–H	0.860(15)	0.860(18)	0.836(16)	0.846(16)	0.859(18)	0.879(18)	0.898(18)
H···O3^{iv}	1.755(16)	1.80(2)	1.799(16)	1.762(16)	1.78(2)	1.73(2)	1.71(2)
O1···O3^{iv}	2.6038(13)	2.604(3)	2.6223(17)	2.5985(17)	2.593(3)	2.579(2)	2.575(2)
O1–H···O3^{iv}	169(2)	155(4)	168(2)	169(2)	158(3)	161(3)	160(3)

[a] Symmetry transformations: i = $-y$, $x-y$, z; iv (for **1–4** and **7**) = $y+2/3$, $x+1/3$, $-z+4/3$, iv (for **10**, and **11**) = $y-2/3$, $x-1/3$, $-z+2/3$. The symmetry transformations for the H-bonds differ for the Δ- and Λ-configuration.

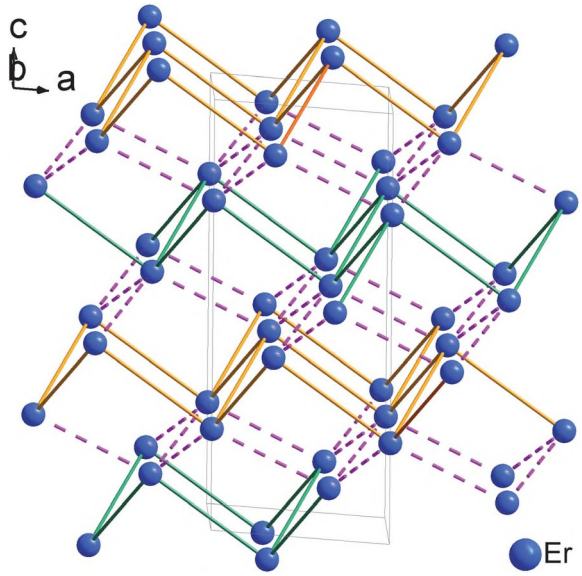

Fig. 4 Schematic representation of the Ln atoms with their covalent and inter-layer hydrogen-bonded topological connectivity (intra-layer H-bonds, *cf.* Fig. 1 and 2, are not shown). Two adjacent (6,3)-nets (differentiated by orange and green topological Ln–Ln connections along the mesoxalate bridges) are connected by inter-layer hydrogen-bonding interactions (dashed pink lines), thus connecting the (6,3)-nets into a 3D supramolecular pcu, α-polonium framework.

hydrogen-bonded framework of the pcu α-Po type (Fig. 4).[56] The 2D homochirality of one layer is transferred through these strong H-bonds to the adjacent layers leading to the overall homochirality of a single crystal.

Crystals of the space group *R*32 should be enantiomorphic and, therefore, manually separable.[57] Unfortunately, crystals with Λ- or Δ-metal-centered chirality looked very similar; separation was not feasible (Fig. S3 in the ESI†). Intermolecular hydrogen bonding interactions result in less dense packing of the building units than may be otherwise possible.[58] There are potential solvent areas calculated by PLATON.[33] For example, for compound **1** the total potential solvent area volume is 234.4 Å^3 per unit cell volume of 1752.5 Å^3 (corresponding to 13.4%, packing index: 70.2% filled space) (see Table S2 in the ESI† for a list of **1–11**). These potential solvent area volumes consist of two crystallographically unique voids. Void(1) is located within the chair-shaped six-membered rings (special position 0, 0, 0) (Fig. 5). Void(2) results from the interdigitation of adjacent layers (Fig. 6, *cf.* Fig. 4) (special position 0, 0, $^1/_2$). Void(2) is smaller than void(1). In each unit cell there are a total of six voids (three of each). Each void packs in a slightly distorted face-centered cubic (fcc) arrangement. Each void type sits in the octahedral interstitial sites of the fcc packing of the respective other void. This combines to a slightly distorted NaCl-type packing of both combined voids(1) and voids(2) (Fig. 7).

The PLATON squeeze function[33] was used solely to determine the electron count in the unit cell. The *hkl*-file generated from "squeeze" was, however, not used for any further refinement. The original *hkl*-file is the file used for refinement of the deposited structures. The total ($F_o - F_c$) map electron count in the unit cell differs from 9 to 16 depending on the measured dataset of **1–10**

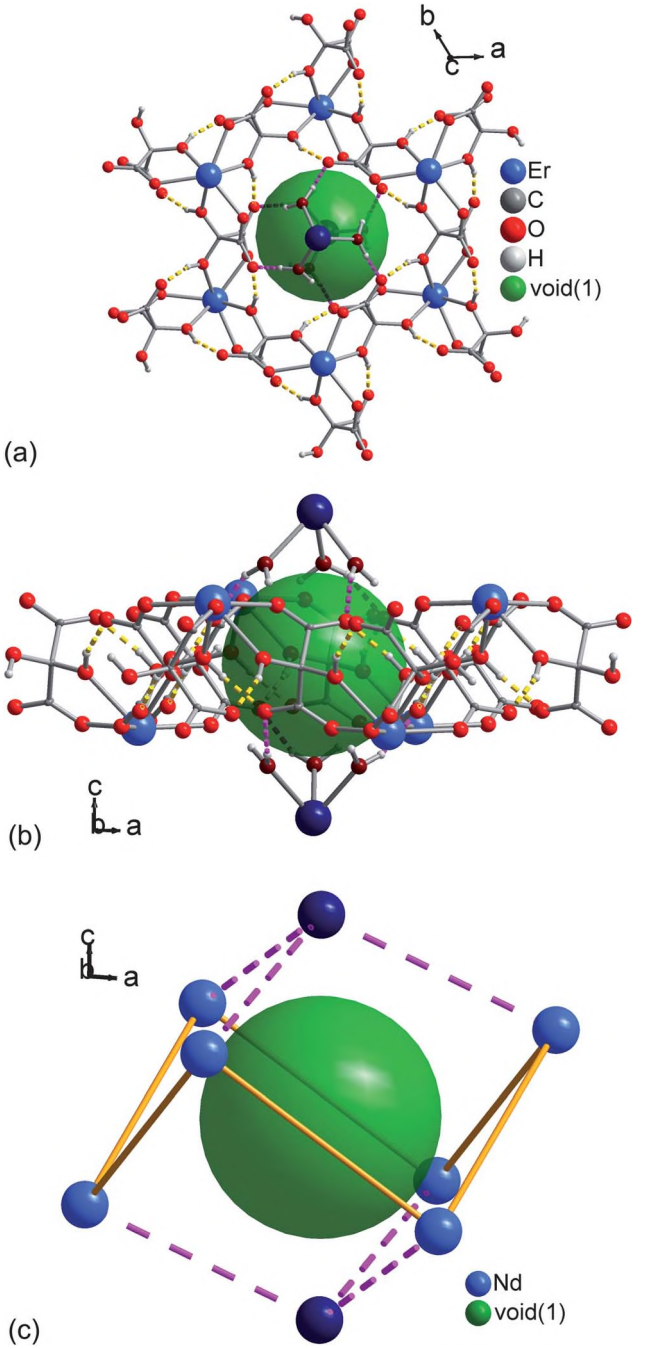

Fig. 5 Hydrogen-bond network surrounding void(1) in compounds **1–11**. The green sphere represents void(1) which is depicted with a space-filling radius of 2.9 Å. For (a) and (b) ball and stick representation of **10**; (c) schematic presentation akin to Fig. 4 with compound **4** (see also Fig. S4 in the ESI†). Dashed yellow lines indicate H-bonds within a layer, dashed pink lines are interlayer hydrogen bonds (*cf.* Fig. 3 and 4). The aqua ligands on the (blue) Er atoms of the central layer are not shown for clarity. The dark-blue Er atoms of the layer above and below are shown with their aqua ligands in (a) and (b), which cap the void by H-bonding. Distances from the void center to the surrounding atoms are given in Table S3 in the ESI†.

(Table 3). This corresponds to roughly 1 to 1.5 H_2O additional molecules or 0.5 to 1 O_2 additional molecule in the unit cell. Five different crystals (a–e) were measured of compound **1** (La). One

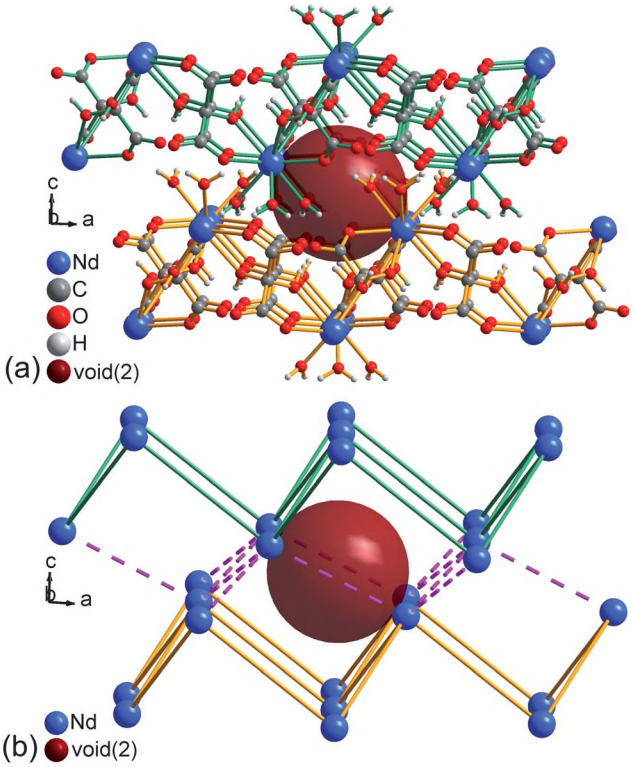

Fig. 6 Layers surrounding void(2) in compounds **1–11**. The dark-red sphere represents void(2) which is depicted with a space-filling radius of 2.9 Å. Compound **4** was chosen as an example (see also Fig. S5 in the ESI†). (a) Ball and stick representation, (b) schematic presentation akin to Fig. 4. Dashed pink lines are interlayer hydrogen bonds (*cf.* Fig. 3 and 4). Distances from the void center to the surrounding atoms are given in Table S3 in the ESI†.

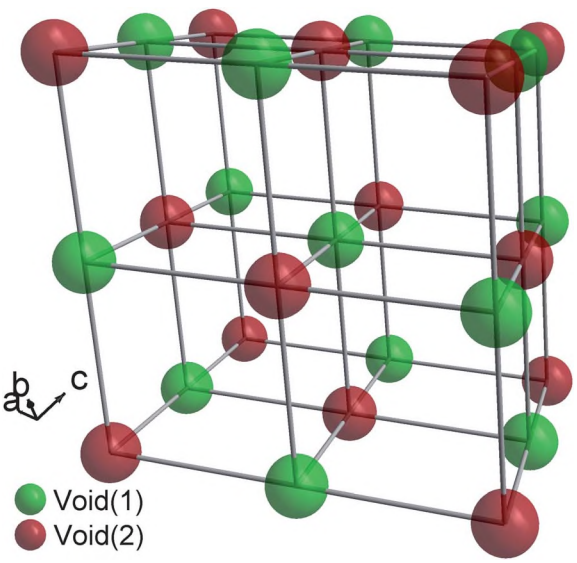

Fig. 7 Slightly distorted NaCl-type packing of voids(1) and voids(2).

crystal was mounted straight out of the mother liquid (see **1**[b] in Table 3). For compound **10** the total electron count here equals exactly one H_2O molecule spread through the six voids in one unit cell. A closer look at the electron density ($F_o - F_c$)-map

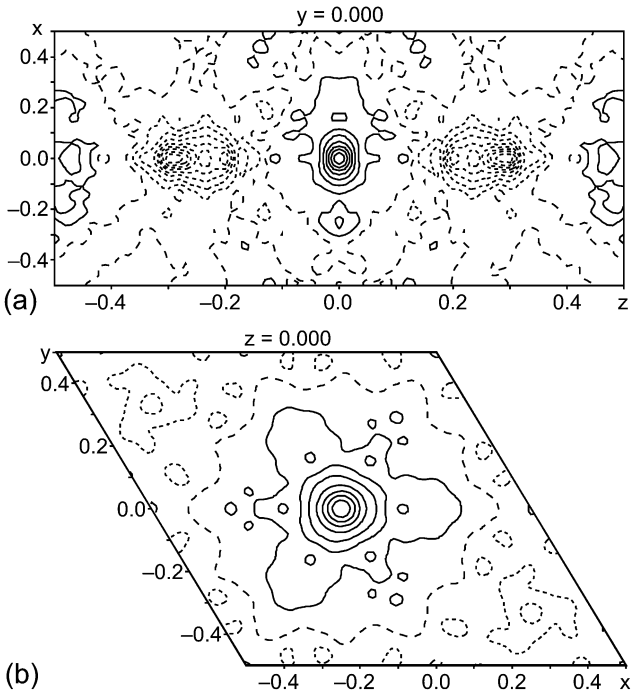

Fig. 8 Residual electron density map $F_o - F_c$ of compound **10** for void (1). At position (0, 0, 0) the electron density is 1.596 eÅ^{-3}; (a) *xz* plane at $y = 0$; (b) *xy* plane at $z = 0$; contour intervals are 0.2 eÅ^{-3}. Positive contours are shown with solid lines and negative contours are shown with dashed lines.

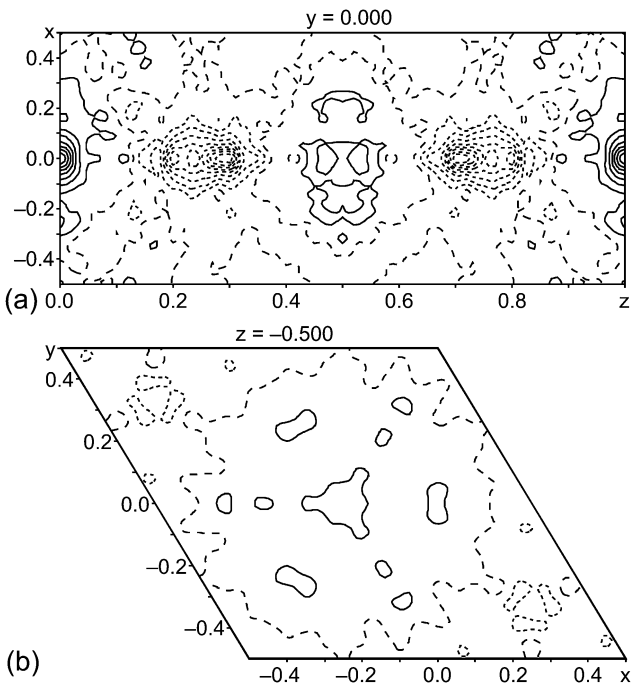

Fig. 9 Residual electron density map $F_o - F_c$ of compound **10** for void (2); at position (0, 0, $^1/_2$) which is in the center of each picture the electron density is 0.226 eÅ^{-3}; (a) *xz* plane at $y = 0$; (b) *xy* plane at $z = -0.5$; contour intervals are 0.2 eÅ^{-3}. Positive contours are shown with solid lines and negative contours are shown with dashed lines.

Table 3 Total potential volume values and total ($F_o - F_c$) map electron count in unit cell values calculated using the squeeze function in PLATON

Compound	Total ($F_o - F_c$) map electron count in unit cell	Total (positive) electron count in voids per cell	Total potential solvent area vol in Å^3	Void vol. per unit cell vol. in %
1[a]	12	12	234.4	13.4
1[b]	7	10	230.9	13.2
1[c]	15	15	232.6	13.3
1[d]	9	12	225.9	12.9
1[e]	6	9	249.6	14.2
2	6	9	235.4	13.6
3	13	13	242.3	13.8
4	8	12	222.1	13.0
7	15	15	215.9	12.9
10	8	11	193.7	11.9
11	16	16	194.9	12.1

[a] Crystal measured at 123 K, submitted structure, *cf.* Table 2. [b] Crystal mounted directly from mother liquid, measured at 223 K. [c] Crystals measured at 243 K. [d] Crystals measured at 243 K. [e] Crystals measured at 243 K.

created with the program Jana2006 shows that localization of these additional electron densities is impossible. No electron density in the shape of a water molecule, nitrogen or oxygen molecule can be identified (see Fig. 8 and 9).

Luminescent properties

The solid-state excitation and emission spectra of the powdered europium (**6**) (Fig. 10a and b) and terbium (**8**) (Fig. 10c and d) complexes were recorded at room temperature. Compound **6** exhibits several strong characteristic excitation bands monitored at 614 nm for isolated europium(III) ions (Fig. 10a) with a maximum at 394 nm (25.4×10^3 cm^{-1}), which is well in the range of excited Eu^{3+} states.[59,60] The emission bands excited at 394 nm peak at 536 ($^5D_1 \rightarrow {}^7F_1$, 18.7×10^3 cm^{-1}), 583 and 592 (both $^5D_0 \rightarrow {}^7F_1$, maximum at 16.9×10^3 cm^{-1}), 614 ($^5D_0 \rightarrow {}^7F_2$, 16.3×10^3 cm^{-1}), 648 nm ($^5D_0 \rightarrow {}^7F_3$, 15.4×10^3 cm^{-1}), the $^5D_0 \rightarrow {}^7F_4$ transition ranges from 684 to 701 nm (around 14.4×10^3 cm^{-1}). The excitation spectrum of the terbium compound monitored at 546 nm shows an optimum excitation at 369 nm (27.1×10^3 cm^{-1}) within a series of intense absorptions between 330 and 390 nm (Fig. 10c). The emission spectrum excited at 369 nm displays the characteristic emission bands for isolated terbium(III) ions as presented in Fig. 10d.[59] These emission bands are found in the visible region at 489 ($^5D_4 \rightarrow {}^7F_6$, 20.5×10^3 cm^{-1}), 541 ($^5D_4 \rightarrow {}^7F_5$, 18.5×10^3 cm^{-1}), 546 ($^5D_4 \rightarrow {}^7F_5$, 18.3×10^3 cm^{-1}), 585 ($^5D_4 \rightarrow {}^7F_4$, 17.1×10^3 cm^{-1}), 606 ($^5D_4 \rightarrow {}^7F_3$, 16.5×10^3 cm^{-1}), 619 nm ($^5D_4 \rightarrow {}^7F_3$, 16.2×10^3 cm^{-1}), 646–649 ($^5D_4 \rightarrow {}^7F_2$, around 15.4×10^3 cm^{-1}), 666 ($^5D_4 \rightarrow {}^7F_1$, 15.0×10^3 cm^{-1}) and 677 ($^5D_4 \rightarrow {}^7F_0$, 14.8×10^3 cm^{-1}). All transitions coincide within a few hundred wavenumbers with those normally observed in an oxygen-dominated environment.[61,62] The excitation wavelengths were chosen according to the maximum excitation recorded for the strongest emission bands. In both cases the excitation spectra suggest that the rare earth ions are directly excited *via* f–f transitions. The dominating intensity of the hypersensitive transition within trivalent europium ($^5D_0 \rightarrow {}^7F_2$), which reacts strongly to the absence of a local inversion centre, reflects nicely and thus proves the chiral environment of the rare earth ions within the complexes.

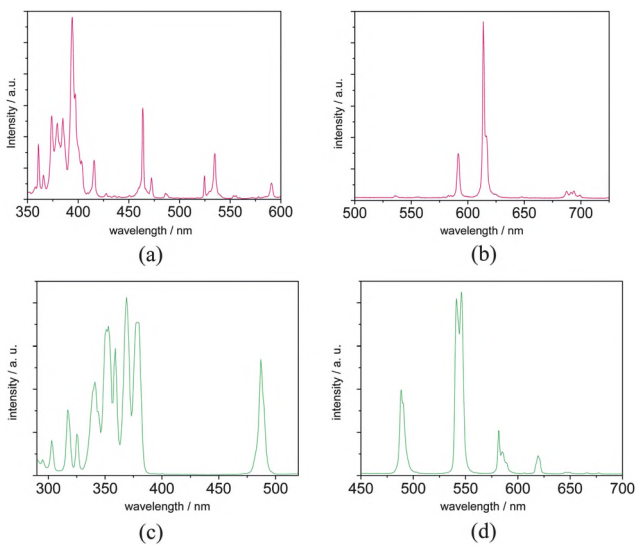

Fig. 10 Solid state excitation spectra of europium mesoxalate (**6**) monitored at 614 nm (a) and of terbium mesoxalate (**8**), monitored at 546 nm (c). Emission spectra from powders of europium ((b), excited at 394 nm) and terbium mesoxalate ((d), excited at 369 nm).

Magnetic properties

The magnetic properties of lanthanoid(III) ions are very different from those of 3d ions; the 4f orbitals are shielded by the fully occupied 5s and 5p orbitals and these $4f^n$ electrons are almost not involved in the bonds between the lanthanoid ion and its nearest neighbours. This makes the energy states of the $4f^n$ configurations to be, in a first approximation, those of the free ions and the influence of the environment is much less pronounced than in the 3d ions (these are the arguments of the so-called free-ion approximation).[63] On the other hand, the spin–orbit coupling has a much larger effect than in the 3d ions and it has to be considered first by applying the Russell–Saunders coupling scheme. This coupling scheme gives rise to the ground and first excited states shown in Table 4 for the lanthanoid(III) ions whose mesoxalates are studied in this work.

The separation in energy between the ground state and the first excited state is (in all but two cases: Sm^{3+} and Eu^{3+}), large enough to consider thermally inaccessible the first excited state and so the

Table 4 Ground, first excited states and energy gap between those states in some lanthanoid(III) ions. Values of g_J for the ions and expected and calculated room temperature $\chi_M T$ values for compounds **1–11**

Lanthanide ion	g_J	Ground state	1st excited state	Energy gap/cm^{-1}	$\chi_M T$ expected/ cm^3 mol^{-1} K	$\chi_M T$ observed/ cm^3 mol^{-1} K
Ce^{3+}	6/7	$^2F_{5/2}$	$^2F_{7/2}$	2200	1.62	1.53
Pr^{3+}	4/5	$^3H_4$	$^3H_5$	2100	3.20	3.18
Nd^{3+}	8/11	$^4I_{9/2}$	$^4I_{11/2}$	1900	3.28	3.25
Sm^{3+}	2/7	$^6H_{5/2}$	$^6H_{7/2}$	167[a]	0.18	0.68
Eu^{3+}	5	$^7F_0$	$^7F_1$	376[a]	4.50	0.00
Gd^{3+}	2	$^8S_{7/2}$	$^6P_{7/2}$	30 000	15.76	15.73
Tb^{3+}	3/2	$^7F_6$	$^7F_5$	2000	23.62	23.31
Dy^{3+}	4/3	$^6H_{15/2}$	$^6H_{13/2}$	3500	28.34	27.86
Er^{3+}	6/5	$^4I_{15/2}$	$^4I_{13/2}$	6500	22.96	22.62
Yb^{3+}	8/7	$^2F_{7/2}$	$^2F_{5/2}$	10 000	5.14	5.21

[a] The value for the calculated spin–orbit coupling parameter, λ, is given.

magnetic properties of the ions are determined solely by the ground state shown in Table 4.[64] Once the effect of the spin–orbit coupling has been considered, the influence of the crystal or ligand field and the magnetic interactions can be taken into account. The ligand field may exhibit any symmetry (cubic, axial or rhombic), which splits the ground term into multiplets. If the width of the multiplets is small enough, the effect of the decrease of the temperature is then the depopulation of the components of higher energy which may result in a deviation from the Curie law, having the same effect as antiferromagnetic interactions. So firstly ground terms and the expected values for the $\chi_M T$ product at room temperature will be calculated and then the temperature dependence of the $\chi_M T$ product will be explained.

The temperature dependence of the $\chi_M T$ product for compounds **2–11** is shown in Fig. 11 and 12. It should be noted that the compounds have two lanthanoid ions and the value of the $\chi_M T$ product is the double of the expected for a single Ln(III) ion. At room temperature all the compounds display values for the $\chi_M T$ product very close to the expected ones and so, the free-ion approximation is good to explain the magnetic behaviour at room temperature (Table 4).

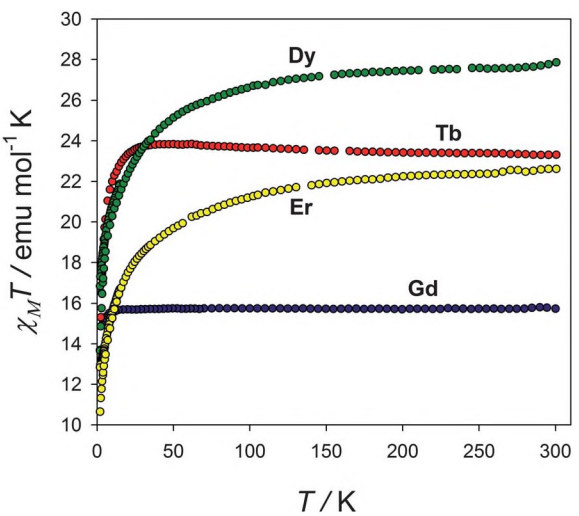

Fig. 11 Temperature dependence of the $\chi_M T$ product for compounds **7–10** (blue, red, green and yellow, respectively).

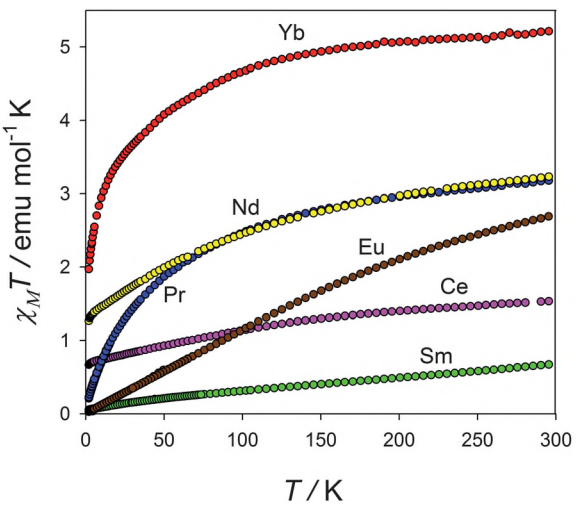

Fig. 12 Temperature dependence of the $\chi_M T$ product for compounds **2–6** and **11** (pink, blue, yellow, green, maroon and red, respectively).

The decrease of the values of the $\chi_M T$ product on lowering the temperature exhibited by most of the compounds can be attributed to the occurrence of antiferromagnetic interactions between the lanthanoid ions or to the loss of the degeneracy of the ground state by the crystal or ligand field. The simplest case is that of Gd(III) ion with the $4f^7$ electronic configuration and it will help to elucidate which of the above mentioned two factors is the most important in the variation of the $\chi_M T$ product on lowering the temperature. Its ground state is the $^8S_{7/2}$, there is no spin–orbit coupling since $L = 0$, the first excited state is 30 000 cm^{-1} above the ground state, the crystal field has no noticeable effect on its magnetic properties and the deviations from the Curie law are only due to magnetic coupling. Additionally the value of the magnetic coupling constant can be calculated by means of a numerical expression for the susceptibility in a bidimensional lattice with a honeycomb structure as observed in Ln(III) mesoxalates.[55,65] Under this approach, the magnetic coupling constant was calculated and only very weak antiferromagnetic interactions were found to occur through the diol bridge [$J = -0.0039$ (1) cm^{-1}], Fig. 13.[20]

The analysis performed for the magnetic susceptibility data of the Gd(III) compound is not possible for the rest of compounds. However, the weak interaction observed must be extrapolable

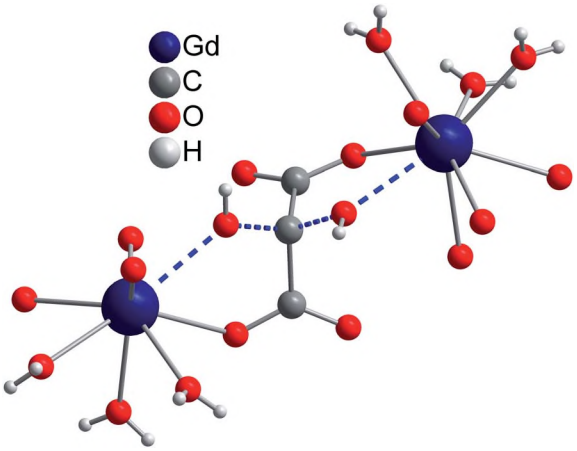

Fig. 13 Magnetic coupling pathway through the diol bridge.

and the considerable decrease of the $\chi_M T$ product found in the rest of compounds cannot be attributed to antiferromagnetic couplings, but to the effect of the crystal field, as in many other Ln(III) compounds. Thus, the depopulation of the components of higher energy is the main cause of the deviation of the $\chi_M T$ product from the Curie law as the temperature is lowered.

For the case of Eu(III), compound **6**, Fig. 14, the ground term ^7F is split into six ^7F_J levels by the spin–orbit coupling, λ, with J ranging from 0 to 6. Since λ is small enough for the first excited state to be thermally populated (around 300 cm^{-1}), the magnetic susceptibility follows the numerical expression given in eqn (1) (ref. 64)

$$\chi = \frac{N\beta^2}{3kTx}\frac{A}{B} \quad (1)$$

with $A = [24 + ((27x - 3)/2)e^{-x} + ((135x - 5)/2)e^{-3x} + (189x - 7/2)e^{-6x} + (405x - 9/2)e^{-10x} + ((1485x - 11)/2)e^{-15x} + ((2457x - 13)/2)e^{-21x}]$ and $B = [1 + 3e^{-x} + 5e^{-3x} + 7e^{-6x} + 9e^{-10x} + 11e^{-15x} + 13e^{-21x}]$ and where N stands for Avogadro's number, β for the Bohr magneton, k the Boltzmann constant, T the temperature, $x = \lambda/kT$ and λ the spin–orbit coupling parameter. Best fit of the magnetic susceptibility data to eqn (1) in the temperature range 50–300 K gives $\lambda = 376$ cm^{-1}, a value in the expected range. The magnetic susceptibility data match very well the theoretical curve in the 50–300 K temperature range. And so, the decrease of the values of the $\chi_M T$ product on lowering the temperature is due to the effect of the spin–orbit coupling. The deviation observed at very low temperatures can be due to weak ferromagnetic interactions between the Eu(III) ions.

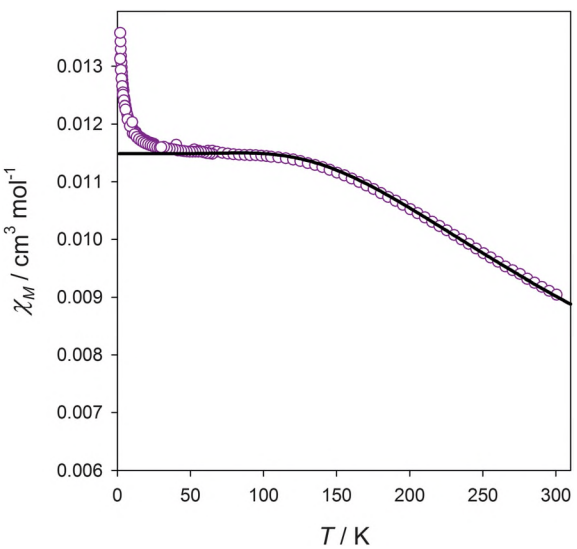

Fig. 14 Temperature dependence of the magnetic susceptibility for compound **6**. The solid line corresponds to the best fit through eqn (1).

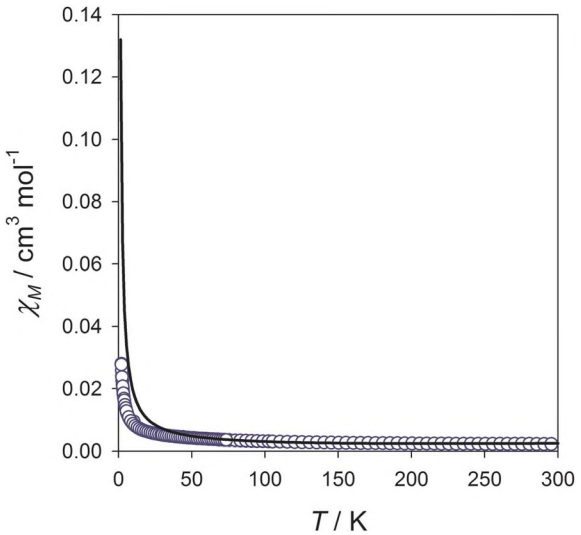

Fig. 15 Temperature dependence of the magnetic susceptibility for compound **5**. The solid line corresponds to the best fit through the model, see text (ref. 63 pp. 49–50).

The ^6H ground term for Sm(III) (Fig. 15) is close in energy to the first excited state and it can be thermally populated at room temperature and above, this causes the deviation of the magnetic susceptibility plot from the Curie law. The expression for the magnetic susceptibility can be found in the literature and from it the value of the spin–orbit coupling parameter can be obtained.[64] The best fit value for the spin–orbit coupling parameter is $\lambda = 167$ cm^{-1}. Values around 200 cm^{-1} are considered as expected and the magnetic susceptibility plot reproduces the theoretical values till 50 K. Below that temperature the experimental magnetic susceptibility values lie below the theoretical ones, this suggests some weak antiferromagnetic couplings amongst the Sm(III) ions.

Conclusions

The achiral mesoxalato ligand (H_2mesox^{2-}) is a new enantiopurity enforcer in extended structures by yielding the homochiral MOFs 2D-[$Ln_2(\mu$-$H_2mesox)_3(H_2O)_6$]. The chirality of the compounds can be observed in the features of the crystal structure and also in the dominating intensity of the hypersensitive transition within trivalent europium ($^5D_0 \rightarrow {}^7F_2$), which reacts strongly to the absence of a local inversion centre and reflects nicely and thus proves the chiral environment of the rare earth ions within the complexes. Compounds **2–11** exhibit the typical magnetic behaviour of lanthanoid(III) ions with deviations from the Curie law mainly owing to the split of the ground term due to the crystal or ligand field, the magnetic coupling being noticeable only at very low temperatures. The magnetic behaviour of the

Eu(III) and the Sm(III) is governed by the spin–orbit coupling and the deviations from the theoretical expression being as well due to the splitting of the ground term at low temperatures together with some magnetic interaction.

Acknowledgements

JS acknowledges Ministerio Español de Ciencia e Innovación through project MAT2010-16891 and Consolider-Ingenio2010, CSD2006-00015and BGH through grant Programa FPI of ACIISI from Gobierno de Canarias and Fondo Social Europeo. The work of CJ was supported by DFG grant Ja466/14-1.

References

1 C. Janiak, *Dalton Trans.*, 2003, 2781–2804.
2 C. Janiak and J. K. Vieth, *New J. Chem.*, 2010, **34**, 2366–2388.
3 W.-H. Zhu, Z.-M. Wang and S. Gao, *Dalton Trans.*, 2006, 765.
4 S. Bobev, P. H. Tobash, V. Fritsch, J. D. Thomson, M. F. Hundley, J. L. Sarrao and Z. Fisk, *J. Solid State Chem.*, 2005, **178**, 2091.
5 J. C. Bünzli and C. Piquet, *Chem. Soc. Rev.*, 2005, **34**, 1048.
6 Y.-Q. Sun, J. Zhang, Y.-M. Chen and G.-Y. Yang, *Angew. Chem., Int. Ed.*, 2005, **44**, 5814.
7 G.-H. Chen, X.-Y. Liu and J. Cheng, *J. Rare Earths*, 2004, **22**, 381.
8 M. D. Allendorf, C. A. Bauer, R. K. Bhakta and R. J. T. Houk, *Chem. Soc. Rev.*, 2009, **38**, 1330–1352.
9 L. Cañadillas-Delgado, O. Fabelo, J. Pasán, F. S. Delgado, M. Deniz, E. Sepulveda, M. M. Laz, M. Julve and C. Ruiz-Pérez, *Cryst. Growth Des.*, 2008, **8**, 1313.
10 L. Cañadillas-Delgado, O. Fabelo, J. Pasán, M. Julve, F. Lloret and C. Ruiz-Pérez, *Polyhedron*, 2010, **29**, 188.
11 M. Hernandez-Molina, C. Ruiz-Pérez, T. López, F. Lloret and M. Julve, *Inorg. Chem.*, 2003, **42**, 5456.
12 A. U. Czaja, N. Trukhan and U. Muller, *Chem. Soc. Rev.*, 2009, **38**, 1284–1293.
13 J.-R. Li, R. J. Kuppler and H.-C. Zhou, *Chem. Soc. Rev.*, 2009, **38**, 1477.
14 K. Matsumoto, K. Suzuki, T. Tsukuda and T. Tsubomura, *Inorg. Chem.*, 2010, **49**, 4717–4719.
15 K. Kim, M. Banerjee, M. Yoon and S. Das, *Function Metal–Organic Frameworks: Gas Storage, Separation and Catalysis, Topics Current Chemistry*, Springer, Heidelberg, 2010, vol. 293, p. 115.
16 L. Ma, C. Abney and W. Lin, *Chem. Soc. Rev.*, 2009, **38**, 1248–1256.
17 G. L. J. A. Rikken and E. Raupach, *Nature*, 1997, **390**, 493.
18 C. Train, R. Gheorghei, V. Krstic, L. M. Chamoreau, N. S. Ovanesyan, G. L. J. A. Rikken, M. Gruselle and M. Verdaguer, *Nat. Mater.*, 2008, **17**, 729.
19 X.-L. Tong, T.-L. Hu, J.-P. Zhao, Y.-K. Wang, H. Zhang and X.-H. Bu, *Chem. Commun.*, 2010, **46**, 8543–8545.
20 B. Gil-Hernandez, H. A. Höppe, J. K. Vieth, J. Sanchiz and C. Janiak, *Chem. Commun.*, 2010, **46**, 8270–8272.
21 B. Gil-Hernández, P. Gili, J. K. Vieth, C. Janiak and J. Sanchiz, *Inorg. Chem.*, 2010, **49**, 7478–7490.
22 J. Sanchiz, J. Pasán, O. Fabelo, F. Lloret, M. Julve and C. Ruiz-Pérez, *Inorg. Chem.*, 2010, **49**, 7880–7889.
23 *CrystalClearSM 1.4.0*, Rigaku Corporation, Tokyo, Japan, 2007.
24 T. Higashi, *ABSCOR*, Rigaku Corporation, Tokyo, Japan, 1995.
25 *APEX2, Data Collection Program for the APEX2 CCD Area-Detector System*, Bruker Analytical X-ray Systems, Madison, Wisconsin, USA, 2006.
26 G. M. Sheldrick, *SADABS, Program for Area Detector Adsorption Correction*, Institute for Inorganic Chemistry, University of Göttingen, Germany, 1996.
27 H. D. Flack, *Acta Crystallogr., Sect. A: Found. Crystallogr.*, 1983, **39**, 876–881.
28 H. D. Flack and G. Bernardinelli, *Acta Crystallogr., Sect. A: Found. Crystallogr.*, 1999, **55**, 908–915.
29 H. D. Flack and G. Bernardinelli, *Chirality*, 2008, **20**, 681–690.
30 H. D. Flack, M. Sadki, A. L. Thompson and D. J. Watkin, *Acta Crystallogr., Sect. A: Found. Crystallogr.*, 2011, **67**, 21–34.
31 G. M. Sheldrick, in *SHELXL-97, Program for the Refinement of Crystal Structure from Diffraction Data*, University of Göttingen, Germany, 1997.
32 G. M. Sheldrick, *Acta Crystallogr., Sect. A: Found. Crystallogr.*, 2008, **64**, 112–122.
33 A. L. Spek, *J. Appl. Crystallogr.*, 2003, **36**, 7–13; A. L. Spek, *PLATON—A Multipurpose Crystallographic Tool*, Utrecht University, Utrecht, the Netherlands; *Windows implementation*: ed. L. J. Farrugia, University of Glasgow, Scotland, Version 40608 (42008), 2008.
34 K. Brandenburg, *Diamond (Version 3.2), Crystal and Molecular Structure Visualization*, ed. K. Brandenburg and H. Putz Gbr, Crystal Impact, Bonn, Germany, 2009, http://www.crystalimpact.com/diamond.
35 D. Mekhatria, S. Rigolet, C. Janiak, A. Simon-Masseron, M. A. Hasnaoui and A. Bengued-dach, *Cryst. Growth Des.*, 2011, **11**, 396–404.
36 A.-C. Chamayou, M. A. Neelakantan, S. Thalamuthu and C. Janiak, *Inorg. Chim. Acta*, 2011, **365**, 447–450.
37 F. Zhuge, B. Wu, L. Dong, J. Yang, C. Janiak, N. Tang and X.-J. Yang, *Aust. J. Chem.*, 2010, **63**, 1358–1364.
38 H. A. Habib, B. Gil-Hernández, K. Abu-Shandi, J. Sanchiz and C. Janiak, *Polyhedron*, 2010, **29**, 2537–2545.
39 B. M. Drašković, G. A. Bogdanović, M. A. Neelakantan, A.-C. Chamayou, S. Thalamuthu, Y. S. Avadhut, J. S. a. d. Günne, S. Banerjee and C. Janiak, *Cryst. Growth Des.*, 2010, **10**, 1665–1676.
40 F. Zhuge, B. Wu, J. Liang, J. Yang, Y. Liu, C. Jia, C. Janiak, N. Tang and X.-J. Yang, *Inorg. Chem.*, 2009, **48**, 10249–10256.
41 E. Redel, C. Röhr and C. Janiak, *Chem. Commun.*, 2009, 2103–2105.
42 E. Redel, M. Fiederle and C. Janiak, *Z. Anorg. Allg. Chem.*, 2009, **635**, 1139–1147.
43 B. Wu, J. Liang, J. Yang, C. Jia, X.-J. Yang, H. Zhang, N. Tang and C. Janiak, *Chem. Commun.*, 2008, 1762–1764.
44 B. Wu, X. Huang, Y. Xia, X.-J. Yang and C. Janiak, *CrystEngComm*, 2007, **9**, 676–685.
45 T. Dorn, A.-C. Chamayou and C. Janiak, *New J. Chem.*, 2006, **30**, 156–167.
46 T. Dorn, C. Janiak and K. Abu-Shandi, *CrystEngComm*, 2005, **7**, 633–641.
47 M. D. Ward, *Chem. Commun.*, 2005, 5838.
48 H. D. Flack, *Helv. Chim. Acta*, 2003, **86**, 905–921.
49 C. Janiak, A.-C. Chamayou, A. K. M. R. Uddin, M. Uddin, K. S. Hagen and M. Enamullah, *Dalton Trans.*, 2009, 3698–3709.
50 M. Enamullah, A. Sharmin, M. Hasegawa, T. Hoshi, A.-C. Chamayou and C. Janiak, *Eur. J. Inorg. Chem.*, 2006, 2146–2154.
51 H. D. Flack, *Acta Crystallogr., Sect. A: Found. Crystallogr.*, 2009, **65**, 371–389.
52 U. Englert, A. Häring, C. Hu and I. Kalf, *Z. Anorg. Allg. Chem.*, 2002, **628**, 1173–1179.
53 I. Kalf, R. Wang and U. Englert, *J. Organomet. Chem.*, 2006, **691**, 2277–2285.
54 I. Kalf, B. Calmuschi and U. Englert, *CrystEngComm*, 2002, **4**, 548–551.
55 V. A. Blatov, M. O'Keeffe and D. M. Proserpio, *CrystEngComm*, 2010, **12**, 44–48.
56 V. A. Blatov and D. M. Proserpio, *Acta Crystallogr., Sect. A: Found. Crystallogr.*, 2009, **65**, 202–212; the three letter symbols proposed by M. O'Keeffe can be retrieved with further information from the Reticular Chemistry Structure Resource database http://rcsr.anu.edu.au/.
57 H. Klapper and T. Hahn, in *International Tables for Crystallography Vol. A*., Kluwer, Dordrecht, 5th edn, 2002, ch. 10.2, Table 10.2.1.1, pp. 804–805.
58 A. I. Kitaigorodskii, *Molecular Crystals and Molecules*, Academic Press, New York, 1973.
59 W. T. Carnall, P. R. Fields and K. Rajnak, *J. Chem. Phys.*, 1968, **49**, 4447–4450.
60 W. T. Carnall, P. R. Fields and K. Rajnak, *J. Chem. Phys.*, 1968, **49**, 4450–4455.
61 A. Sonnauer, C. Näther, H. A. Höppe, J. Senker and N. Stock, *Inorg. Chem.*, 2007, **46**, 9968–9974.
62 H. A. Höppe, K. Kazmierczak, S. Kacprzak, I. Schellenberg and R. Pöttgen, *Dalton Trans.*, 2011, **40**, 9971–9976.
63 L. Sorace, C. Benelli and D. Gatteschi, *Chem. Soc. Rev.*, 2011, **40**, 3092–3104.
64 O. Kahn, *Molecular Magnetism*, VCH, New York, 1993.
65 R. Navarro, in *Magnetic Properties of Layered Transition Metal Compounds*, ed. L. J. de Jonhg, Kluwer Academic Publishers, The Netherlands, 1990, pp. 105–190.